Materials and Design 191 (2020) 108585

Contents lists available at ScienceDirect

Materials and Design

journal homepage: www.elsevier.com/locate/matdes

Theoretical transmissions for X-ray computed tomography studies of lithium-ion battery cathodes

T.M.M. Heenan *, C. Tan, A.J. Wade, R. Jervis, D.J.L. Brett, P.R. Shearing *

Electrochemical Innovation Lab, Department of Chemical Engineering, UCL, London, WC1E 7JE, UK
The Faraday Institution, Quad One, Harwell Science and Innovation Campus, Didcot OX11 0RA, UK

HIGHLIGHTS

- A methodology for X-ray image optimisation has been outlined for battery materials.
- For optimal cathode image contrast 14% X-ray transmission should be targeted.
- Cathode thickness should be double the inverse of the attenuation coefficient.
- Deviations from theoretical predictions are outlined for real-world scenarios.
- To aid reader's future X-ray experiments a quick-reference guide is presented.

GRAPHICAL ABSTRACT

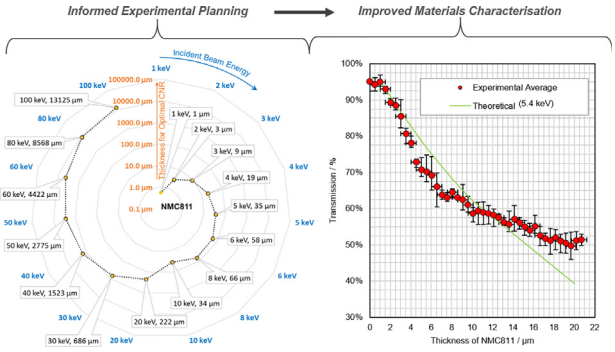

ARTICLE INFO

Article history:
Received 8 November 2019
Received in revised form 17 February 2020
Accepted 19 February 2020
Available online 20 February 2020

Keywords:
Battery
Electrode
Microstructure
X-ray computed tomography
NMC
X-ray attenuation

ABSTRACT

X-ray computed tomography (CT) has emerged as a powerful tool for the 3D characterisation of materials. However, in order to obtain a useful tomogram, sufficient image quality should be achieved in the radiographs before reconstruction into a 3D dataset. The ratio of signal- and contrast-to-noise (SNR and CNR, respectively) quantify the image quality and are largely determined by the transmission and detection of photons that have undergone useful interactions with the sample. Theoretical transmission can be predicted if only a few variables are known: the material chemistry and penetrating thickness e.g. the particle diameter. This work discusses the calculations required to obtain transmission values for various $Li(Ni_XMn_YCo_Z)O_2$ (NMC) lithium-ion battery cathodes. These calculations produce reference plots for quick assessment of beam parameters when designing an experiment. This is then extended to the theoretical material thicknesses for optimum image contrast. Finally, the theoretically predicted transmission is validated through comparison to experimentally determined values. These calculations are not exclusive to NMC, nor battery materials, but may be applied as a framework to calculate various sample transmissions and therefore may aid in the design and characterisation of numerous materials.

1. Introduction

Lithium-ion batteries (LIBs) rely upon complex microstructures in order to safely deliver power for sufficient duration without the requirement of frequent recharging or premature replacement. A combination of the increasing demand for LIBs and the need for ever-improving cell performance has resulted in considerable academic and commercial interest in new cell chemistries. Specifically for the cathode, nickel-rich

* Corresponding authors at: Electrochemical Innovation Lab, Department of Chemical Engineering, UCL, London WC1E 7JE, UK.
E-mail addresses: t.heenan@ucl.ac.uk (T.M.M. Heenan), p.shearing@ucl.ac.uk (P.R. Shearing).

https://doi.org/10.1016/j.matdes.2020.108585

chemistries in the form of $LiNi_XMn_YCo_ZO_2$ or NMC (where x ≥ 0.5) promise desirable reversible capacities and rate capabilities; however, much work is still to be done in overcoming thermal and voltage instabilities and adverse surface reactions [1]. As a result, various approaches are being pursued in order to mitigate degradation, and due to the complexity of the issues, a range of characterisation techniques are required.

X-ray computed tomography (CT) has revolutionised the characterisation of LIB structures [2,3]; 2D methods such as scanning electron microscopy (SEM) are unable to reveal sub-surface detail [4,5] and although internal details can be obtained by removing the surface using, for example, a focused-ion beam (FIB), these methods are destructive, preventing the repeated analysis of the sample and therefore, by definition, precluding time-resolved and operando investigations [6,7]. Laboratory-based instruments are capable of producing spatial resolutions comparable to those achievable at specialist synchrotron facilities [8,9]. However, although considerable improvements have been made with respect to laboratory-based spatial resolutions, temporal limitations remain a hindrance; the brilliance of an X-ray beam from a synchrotron source can be expected to be orders of magnitude higher than a laboratory-based system [10]. As a result, efforts have been made to optimise sample preparation in order to minimise the unnecessary attenuation of the beam [11,12], maximising the contrast- and signal-to-noise ratios (CNR and SNR, respectively). Moreover, in situ and operando investigations have required the design of bespoke cell housings in order to charge and discharge battery materials while still achieving sufficient image quality [13].

Attenuation of the beam intensity as X-ray photons pass through a medium is well described within the literature and forms the basis of absorption-based CT [14]. References are available for element-specific attenuation data for various incident beam energies [15,16], however complex composite material chemistries are the likely candidates for next-generation LIBs, such as the aforementioned NMC cathode. With respect to the CNR ratio, it has been stated that the theoretical optimum for transmission during absorption-based imaging can be expected around 14% [17]. It is therefore valuable to be able to predict transmission values with some degree of accuracy when planning an experiment, something that is not easily possible using the currently available single-element transmission data.

This work outlines the methodology for the calculation of theoretical transmission values for various NMC chemistries, comparing two well-established sources of attenuation data authored by Henke et al. and Hubbell et al. [15,16]. Here, four reference plots are presented as guides for imaging NMC111, 532, 622 and 811; accompanied by the material thickness for optimum image contrast for NMC811. These methods are not limited to NMC, nor LIBs, but may be applied to the wider field of materials analysis using X-ray imaging. We expect that the data presented will be a useful reference for battery researchers, whilst the methodology that is articulate will have wider interests across materials science and engineering fields. Ultimately, the careful planning of experiments will lead to further understanding of materials properties, thus intelligent design and improved performance during application.

2. Materials and methods

2.1. Defining X-ray transmission

The X-ray photon transmission (T) can be defined as the ratio of the transmitted (I) and the incident beam intensities (I_0), as seen in Eq. (1).

$$T = {}^{I}/_{I_0} \tag{1}$$

The transmitted intensity is a function of the medium that the photon passes through; each material has an element-specific X-ray linear attenuation coefficient (μ) for each incident energy (E_0), i.e. $\mu = f(E_0, element)$. The X-ray linear attenuation coefficient dictates the rate of decay of the incident photon intensity via an exponential relationship. This is based upon the Beer-Lambert law and is described in Eq. (2) as the transmitted intensity after passing through a medium of a defined thickness (t).

$$I = I_o.e^{-\mu(E_0).t} \tag{2}$$

2.2. X-ray mass attenuation coefficients

Eqs. (1) and (2) can be combined in order to predict the photon transmission through a certain thickness of a particular medium, e.g. X-ray transmission through a battery. Often the medium of interest (e.g. a battery) contains several materials (e.g. electrode, electrolyte, separator), each composed of several elements (e.g. an electrode that contains *O*, *Ni*, *Mn*, *Co* and *Li*). Furthermore, as described by Hubbell et al. [16] in Eq. (3), the X-ray mass attenuation coefficient of a compound (μ_m) can be calculated by the sum of the X-ray mass attenuation coefficients of the constituent elements (e.g. $i = Ni, Mn, Co$) multiplied by their weight fractions (w_i).

$$\mu_m(E_0) = \sum_i \left[w_i.\mu_m(i, E_0)\right] \tag{3}$$

2.3. X-ray linear attenuation coefficients

The X-ray linear attenuation coefficient (μ) can be calculated by the product of the X-ray mass attenuation coefficient (μ_m) and the crystallographic density (ρ) of the material, Eq. (4).

$$\mu(E_0) = \mu_m(E_0).\rho \tag{4}$$

For this work, one value for crystallographic density is used for each chemistry, these are summarised in Table 1.

2.4. X-ray attenuation lengths

Rather than the X-ray linear attenuation coefficients, other sources [15] quote the X-ray attenuation length (λ), which is inversely proportional to the linear attenuation coefficient (μ), Eq. (5).

$$\lambda(E_0) = \mu(E_0)^{-1} \tag{5}$$

2.5. Calculating X-ray transmission

Using references for either the X-ray mass attenuation coefficients (μ_m) with crystallographic densities (ρ), or X-ray attenuation lengths (λ), the transmission (T) can be calculated for a defined thickness of material (t) using Eq. (6), i.e. the combination of Eqs. (1), (2) and (5).

$$T = e^{-t.\mu(E_0)} = e^{\frac{-t}{\lambda(E_0)}} \tag{6}$$

2.6. Defining SNR and CNR

Thus far, a quantitative description for transmission has been established with respect to material parameters such as thickness and the attenuating properties for a particular incident X-ray energy, however, this is only useful if this can be translated to real data in the form of image quality. Two common ratios for quantifying image quality are the aforementioned SNR and CNR. These can be defined by Eqs. (7) and (8). For X-ray CT imaging the signal intensity (I) would typically be the greyscale within the radiographs or tomograms, where the

Table 1
Crystallographic densities, in $g\ cm^{-3}$ for four NMC chemistries from various references (to 2 d.p) [18–21].

	NMC111	NMC532	NMC622	NMC811
Chemistry	$LiNi_{0.1}Mn_{0.1}Co_{0.1}O_2$	$LiNi_{0.5}Mn_{0.3}Co_{0.2}O_2$	$LiNi_{0.6}Mn_{0.2}Co_{0.2}O_2$	$LiNi_{0.8}Mn_{0.1}Co_{0.1}O_2$
ρ	4.74	4.72	4.75	4.80

denominator is the standard deviation (σ_g) of the greyscale. When considering the CNR, one feature must be compared with respect to another e.g. feature *a* versus feature *b*, or I_a and I_b, with a ratio taken of their difference to the standard deviaiton of the background (σ_b).

$$SNR = \frac{\bar{I}}{\sigma_g} \tag{7}$$

$$CNR = \frac{I_a - I_b}{\sigma_b} \tag{8}$$

The SNR will generally be governed by the suitability of the instrument for the characterisation of the features of interest, e.g. spatial resolution, beam brilliance; however, may also be improved through increased exposure times. Furthermore, the CNR can be maximized through optimal sample preparation.

2.7. Calculating CNR

Reiter et al. practically translated the CNR into terms of transmission [17]. This first involves generating a relationship to describe contrast variation with respect to small changes in sample thickness (Δt). Initially, one has to differentiate Eq. (2) with respect to thickness, Eq. (9), which produces Eq. (10).

$$\frac{\delta I}{\delta t} = \frac{\delta}{\delta t}\left(I_0.e^{-\mu(E_o).t}\right) \tag{9}$$

$$\frac{\Delta I}{\Delta t} = -I.\mu(E_o) = -I_o.e^{-\mu(E_o).t}.\mu(E_o) \tag{10}$$

Then contrast (C) is defined as the change in the transmitted intensity, producing Eq. (11).

$$C = \Delta I = I_o.e^{-\mu(E_o).t}.\mu(E_o).\Delta t \tag{11}$$

The photon noise detected by an ideal detector (σ) can be defined as the square root of the transmitted intensity, as discussed by Rousseua et al. who also explore non-ideal situations [22], Eq. (12).

$$\sigma = \bar{I}^{\frac{1}{2}} \tag{12}$$

And taking the ratio of the contrast to the photon noise produces the CNR, Eq. (13).

$$CNR = \frac{C}{\sigma} = \frac{I_o.e^{-\mu(E_o).t}.\mu(E_o).\Delta t}{\left(I_o.e^{-\mu(E_o).t}\right)^{\frac{1}{2}}} \tag{13}$$

which can be further simplified to Eq. (14).

$$CNR = \left(I_o.e^{-\mu(E_o).t}\right)^{\frac{1}{2}}\mu(E_o).\Delta t \tag{14}$$

Retier et al. also discuss how the CNR reaches a theoretical maximum when the first derivative of Eq. (14), i.e. Eq. (15), equals zero, producing Eq. (16).

$$\frac{\delta CNR}{\delta \mu} = \frac{\delta}{\delta \mu}\left(\Delta t.\left(I_o.e^{-\mu(E_o).t}\right)^{\frac{1}{2}\mu(E_o)}\right) \tag{15}$$

$$\frac{\delta CNR}{\delta \mu} = \Delta t.\left(I_o.e^{-\mu(E_o).t}\right)^{\frac{1}{2}}.\left(1 - \frac{\mu(E_o).t}{2}\right) = 0 \tag{16}$$

which simplifies into the concise relationship, Eq. (17).

$$t.\mu(E_o) = 2 \tag{17}$$

Simply, Eq. (17) can be interpreted thus: the theoretical sample thickness for optimum image contrast can be found when the product of the X-ray linear attenuation coefficient and the thickness equals two. This would be true for all materials under the aforementioned assumptions.

2.8. Optimal imaging for maximal CNR

Finally, combining Eqs. (6) and (17) and solving for transmission produces Eq. (18), the theoretical transmission for optimal image contrast, which is equal to 14%.

$$T = e^{-\mu(E_o).t} = e^{\frac{-\mu(E_o)}{\mu(E_o)}.2} = e^{-2} \sim 14\% \tag{18}$$

2.9. Material

A $LiNi_{0.8}Mn_{0.1}Co_{0.1}O_2$ cathode powder purchased from a commercial supplier (Targray Inc., Kirkland, Canada) was used for the experimental validation of this work. The dark powder was dispersed over a white tile, then a thin layer of epoxy was applied to the tip of a sharp steel pin. The pin was lowered to the tile and a very small amount of powder was immobilised to the pin head (several particles).

2.10. X-ray imaging

The X-ray data was collected using a lab-based Zeiss Xradia 810 Ultra X-ray instrument (Carl Zeiss inc., CA, USA). This instrument employs a quasi-monochromatic 5.4 keV, parallel-beam geometry coupled to a Fresnel zone plate focusing architecture. Radiographs of the pin and

Table 2
X-ray mass attenuation coefficients calculated from elemental data tables by Hubbell et al. [16] for four NMC chemistries from 1 to 100 keV, presented in units of $cm^2\ g^{-1}$ *(to 1 d.p.)*.

Incident energy, E_0/keV	X-ray mass attenuation coefficient, $\mu_m(E_0)/cm^2\ g^{-1}$			
	111	532	622	811
1	7056.5	7110.6	7221.1	7333.7
2	1277.3	1314.8	1353.2	1407.5
3	432.3	445.7	459.5	478.9
4	197.2	203.4	209.9	219.0
5	106.5	110.0	113.6	118.6
6	64.2	66.4	68.5	71.6
8	131.5	105.3	92.4	62.9
10	110.2	113.8	117.5	122.6
20	16.8	17.4	18.0	18.8
30	5.4	5.6	5.8	6.1
40	2.4	2.5	2.6	2.7
50	1.3	1.4	1.4	1.5
60	0.9	0.9	0.9	0.9
80	0.4	0.5	0.5	0.5
100	0.3	0.3	0.3	0.3

Table 3
X-ray mass attenuation coefficients calculated from elemental data tables by Henke et al. [15] for four NMC chemistries from 1 to 30 keV, presented in units of $cm^2\ g^{-1}$ *(to 1 d.p.)*.

Incident energy, E_0/keV	X-ray mass attenuation coefficient, $\mu_m(E_0)/cm^2\ g^{-1}$			
	111	532	111	811
1	7144.1	7266.1	7417.7	7611.1
2	1260.7	1295.6	1332.3	1383.4
3	419.0	432.2	445.6	464.7
4	190.8	197.5	204.0	213.5
5	102.3	106.2	109.8	115.1
6	61.4	63.8	65.9	69.1
8	129.6	103.6	90.6	61.3
10	108.7	112.4	116.0	121.2
20	16.0	16.7	17.3	18.1
30	5.1	5.3	5.5	5.8

NMC particles, with a field of view of 64 μm × 64 μm, were collected for 141 projections with an exposure time of 1 s per projection for a pixel size of ca. 500 nm. This data was then reconstructed into a tomogram using commercial software ('Reconstructor Scout-and-Scan', Carl Zeiss Inc., CA, U.S.A.). The transmission was calculated as the ratio of the detector counts for a particular pixel with and without the sample. The thickness was calculated from the reconstructed tomogram by taking the beam path from the corresponding radiograph pixel and measuring the number of pixels that contain NMC within that path and multiplying by the pixel length.

3. Results

3.1. Comparing two data sources

This report will begin by describing how to use the comprehensive data libraries published by Hubbell and Henke et al. [15,16]. The two sources will then be compared, to examine the degree of their corroboration.

Hubbell et al. [16] report the X-ray mass attenuation coefficients for elements with atomic numbers from 1 to 92 and X-ray energies from 1 keV to 20 MeV. As mentioned within the introduction, LIB materials that fulfill all of the necessary performance requirements, such as NMC, often require complex chemistries consisting of several elements, *Ni*, *Mn*, *Co*. Therefore the elemental data reported by Hubbell must be used in combination with Eq. (3) to produce values for practical materials. The Hubbell reference data can be used to calculate the X-ray mass attenuation coefficients for NMC using Eq. (3). The results are presented in Table 2. It should be noted that absorption edges significantly influence X-ray properties as can be seen in the transition between incident energies of 6 to 8 k eV in Table 2.

Additional sources are available for element-specific X-ray attenuation properties; Henke et al. provide X-ray attenuation lengths for energies between 50 and 30,000 eV for atomic numbers from 1 to 92 [15]. To directly compare this data with the previous reference [16], Eqs. (3), (4) and (5) were used to calculate the X-ray mass attenuation coefficients, the results are presented in Table 3.

In order to compare and validate the data obtained from the two references [15, 16], Fig. 1 presents the X-ray mass attenuation coefficients

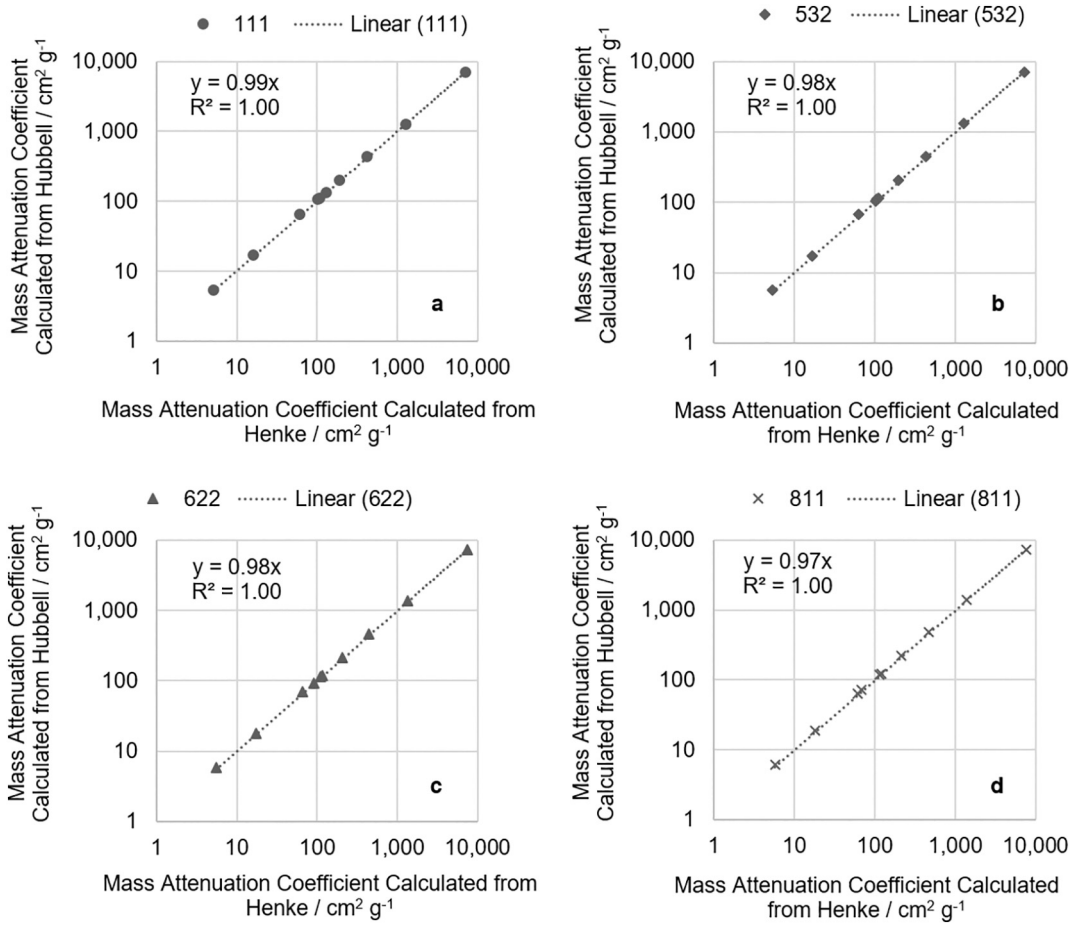

Fig. 1. Comparing the X-ray mass attenuation coefficients for energies from 1 to 30 keV for various NMC chemistries calculated from two references: a) NMC111, b) NMC532, c) NMC622 and d) NMC811 [15,16].

Table 4
X-ray mass attenuation coefficients at 1 keV for four NMC chemistries calculated from references, presented in units of $cm^2\ g^{-1}$ (to 1 d.p.) [15,16].

Starting reference	X-ray mass attenuation coefficient, $\mu_m(E_0)/cm^2\ g^{-1}$			
	111	532	622	811
Henke [15]	7056.5	7110.6	7221.1	7333.7
Hubbell [16]	7144.1	7266.1	7417.7	7611.1

Table 5
Degree of corroboration for X-ray mass attenuation coefficients calculated for four NMC chemistries (to 2 d.p.) [15,16].

Chemistry	Gradient, m/no units	Coefficient of determination, R/no-units
NMC111	0.99	1.00
NMC532	0.98	1.00
NMC622	0.98	1.00
NMC811	0.97	1.00

from the two sources (i.e. Table 2 vs. Table 3), for the four NMC chemistries. Within Fig. 1 there are four sub-plots, one for each of the NMC chemistries, comparing values from 1 to 30 keV. Each datum is calculated for the same energy, allowing for direct comparison (see Table 4 for an example at 1 keV). Hence, plotting the two data sets and performing a linear fitting produces a gradient that would equal unity for a perfect correlation.

Table 5 summarises the gradients and coefficients of determinations for a linear fitting through each of the four plots within Fig. 1. Since the gradients are all very close to unity: 0.99, 0.98, 0.98 and 0.97, for NMC111, NMC532, NMC622 and NMC811 respectively; it can be concluded that the two sources corroborate each other reasonably well and sufficient confidence can be placed in the validity of the attenuation calculations based from either reference.

3.2. Theoretical X-ray transmissions through NMC

X-ray mass attenuation coefficient data (i.e. Tables 2 or 3) can now be converted to X-ray linear attenuation coefficients using Table 1 and Eq. (4). And from this, the transmission can now be calculated using

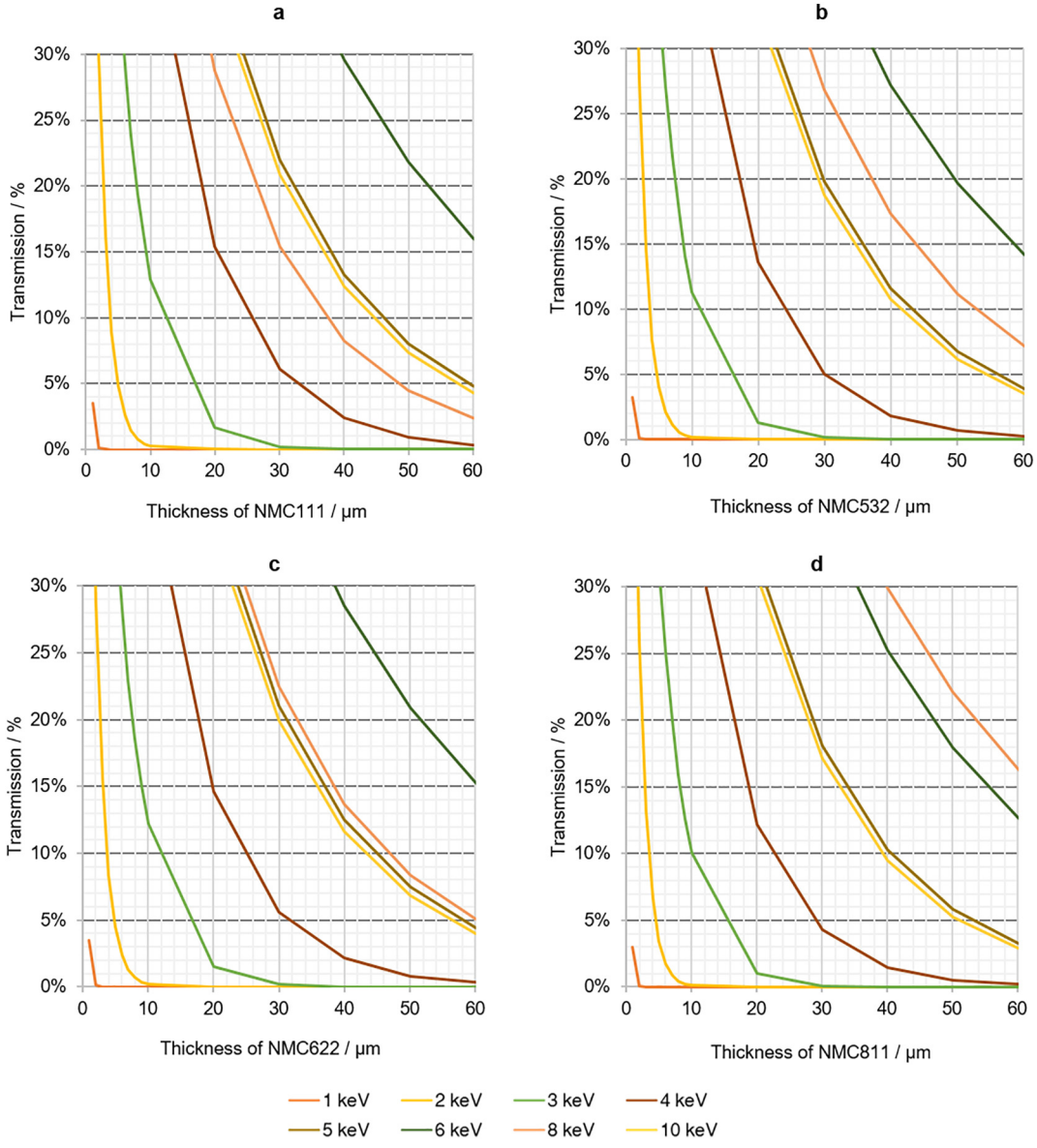

Fig. 2. Expected X-ray transmission through NMC for various thicknesses and incident photon energies: a) NMC111, b) NMC532, c) NMC622 and d) NMC811.

Eq. (19), reproduced below:

$$T = e^{-t.\mu(E_0)} \tag{19}$$

As the transmission is thickness dependant, only thicknesses thought to be relevant to NMC experiments are reported here: 1–60 μm; however, in the complimentary Data in Brief article we report wider thickness and energy ranges [[23] - DiB Article].

Fig. 2 displays transmission values that are below 30% for all thicknesses up to 60 μm. This transmission range has been chosen due to the benefits of imaging at relatively low transmission (10–20%) for optimal image contrast; furthermore, electrode particles generally are smaller than 60 μm in diameter, therefore these ranges should cover most applications. Optimizing transmission for maximal image contrast will be discussed later within the text. The raw data is also tabulated for all incident beam energies from 1 to 100 keV, for thicknesses of 1–100 μm and the four chemistries; which is all supplied within the supplementary Data in Brief article [[23] - DiB Article].

3.3. Optimal samples for maximal contrast

These calculations allow experiments to be intelligently planned in order to optimise image contrast, ultimately maximising the usefulness of the data acquisition and minimising unnecessary use of, what are typically, expensive instruments. Fig. 3 outlines an example of a quick reference guide that may be produced from these calculations: a plot of theoretical thickness with respect to a monochromatic incident beam energy for a dense and lithiated NMC811 particle.

The optimum sample thickness for maximum image contrast (t) has been defined according to Eq. (20). Whereby the optimum thickness is the inverse of half of the X-ray attenuation coefficient (μ), for a particular incident X-ray energy (E_0). For the full derivation, i.e. Eqs. (7)–(16) see the Materials and Methods sections.

$$t.\mu(E_o) = 2 \tag{20}$$

3.4. Specific beam energies

Although tables provide element-specific X-ray mass attenuation coefficients for many energies, values are commonly supplied to the nearest keV. Whereas, calculations are often required for very specific values, particularly for experiments employing a laboratory-based source; this is because the laboratory-based X-rays are typically produced by bombarding an anode target with electrons, producing characteristic X-rays that are specific to the anode material. A linear interpolation assumption produces a reasonable approximation in most instances, provided that there is not an X-ray edge between the two energy values that would cause significant deviation from linearity. For instance, a Zeiss Ultra 810 employs a chromium (Cr) anode target which, after refinement, produces a quasi-monochromatic, 5.4 keV

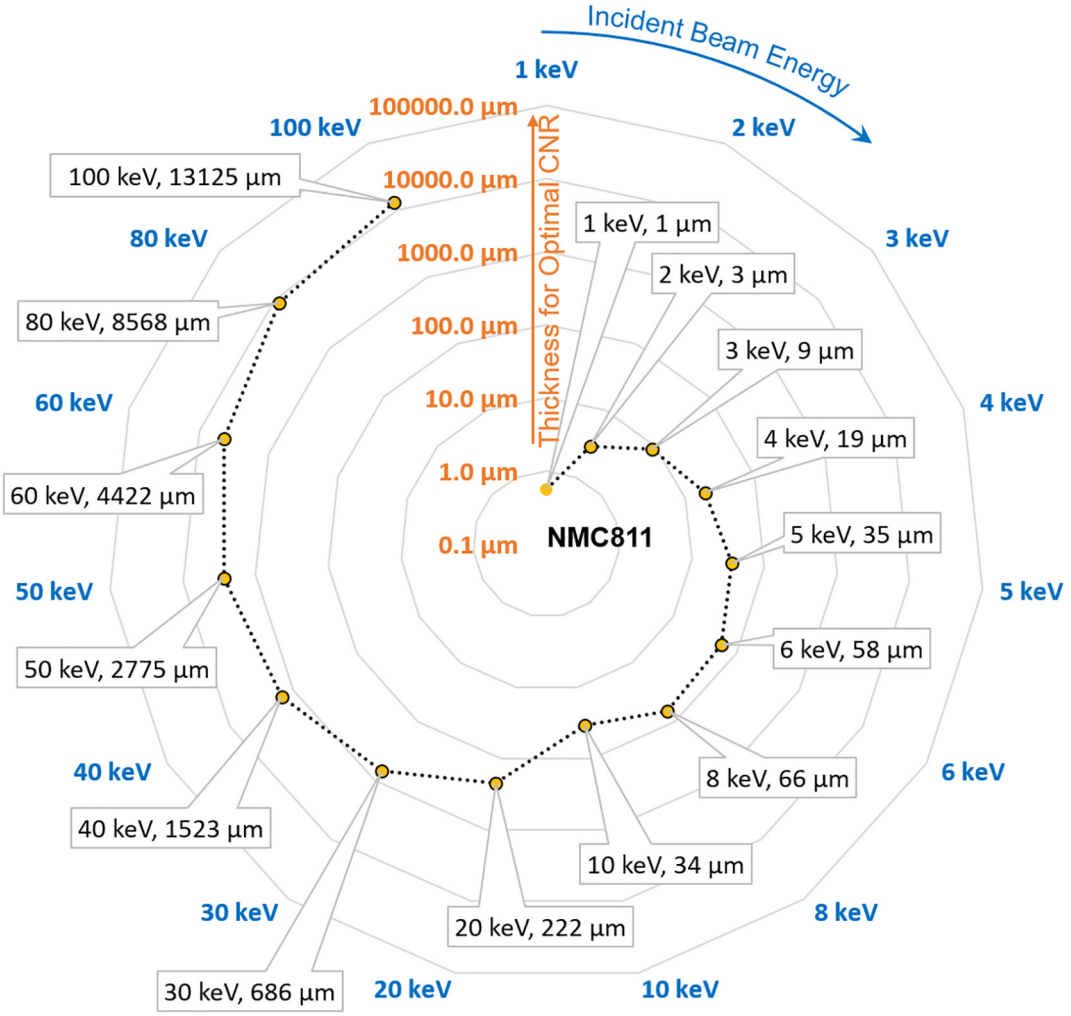

Fig. 3. The application of transmission optimisation: Theoretical thicknesses of NMC811 material for the optimum CNR for various incident beam energies from 1 to 100 keV.

Table 6
Example calculation of the X-ray mass attenuation coefficient values for the constituent elements within NMC for a 5.4 keV characteristic X-ray beam typical of a Cr anode target used within a laboratory-based X-ray source, presented in $cm^2\,g^{-1}$ (to 2 d.p.).

Incident energy, E_o/keV	*Li*	*Ni*	*Mn*	*Co*	*O*	Source
5.0	0.15	179.30	121.20	151.50	47.90	[16]
5.4	0.15	151.18	102.12	128.38	39.82	Calculated
6.0	0.14	109.00	73.50	93.70	27.70	[16]

beam. For this, the 5.0 keV and 6.0 keV X-ray mass attenuation references within Table 1 can be used to calculate a linear interpolation to 5.4 keV. Table 6 presents an example calculation for such a situation.

3.5. Degree of mono-chromaticity

An important assumption throughout these calculations is that the beam is perfectly monochromatic, i.e. it can be described by one single wavelength rather than a distribution of wavelengths. If a beam profile is known, i.e. photon counts with respect to the incident energy or wavelength, a more accurate approximation can be calculated by integrating with respect to the intensity of the contributing wavelengths. Although, this is often not necessary when using rough approximations for experiment preparations, particularly those involving synchrotron radiation.

3.6. Density and composition

Another assumption in these calculations is that the material is perfectly dense (Fig. 4a) and the transmission loss due to the surrounding air is negligible due to reference corrections. Outside of a vacuum, the beam will be attenuated and scattered even by the air between the source-to-sample and sample-to-detector. Contributions to transmission loss by air are typically negligible; however, it becomes increasingly significant at low energies, e.g. important for techniques such as X-ray fluorescence. For instance, for incident photon energies on the order of single electron volts, the attenuation length of air is tens of microns; however, at hundreds of electron volts, this rises to millimetres and at kilo electron volts it is on the order of meters, i.e. approximately seven orders of magnitude less attenuating than metallic elements. Consequently, the relative lack of beam attenuation in air compared to typical battery materials means that any void-space or pores within the sample can increase the net transmission considerably. For example, a completely dense NMC811 particle that is 30 μm in diameter will result in a ca. 76% transmission for a 20 keV beam; whereas, the same particle with 20% internal porosity will produce an 81% transmission. Apart from the internal porosity within the NMC particles, similar implications would arise within a printed electrode sheet, which may constitute: pores, a conductive carbon additive and binder (i.e. the carbon and binder domain - CBD) and electrode particles (e.g. NMC). The NMC content (by volume) may be 30% within a printed electrode, which would considerably increase the X-ray transmission when compared to imaging NMC particles alone.

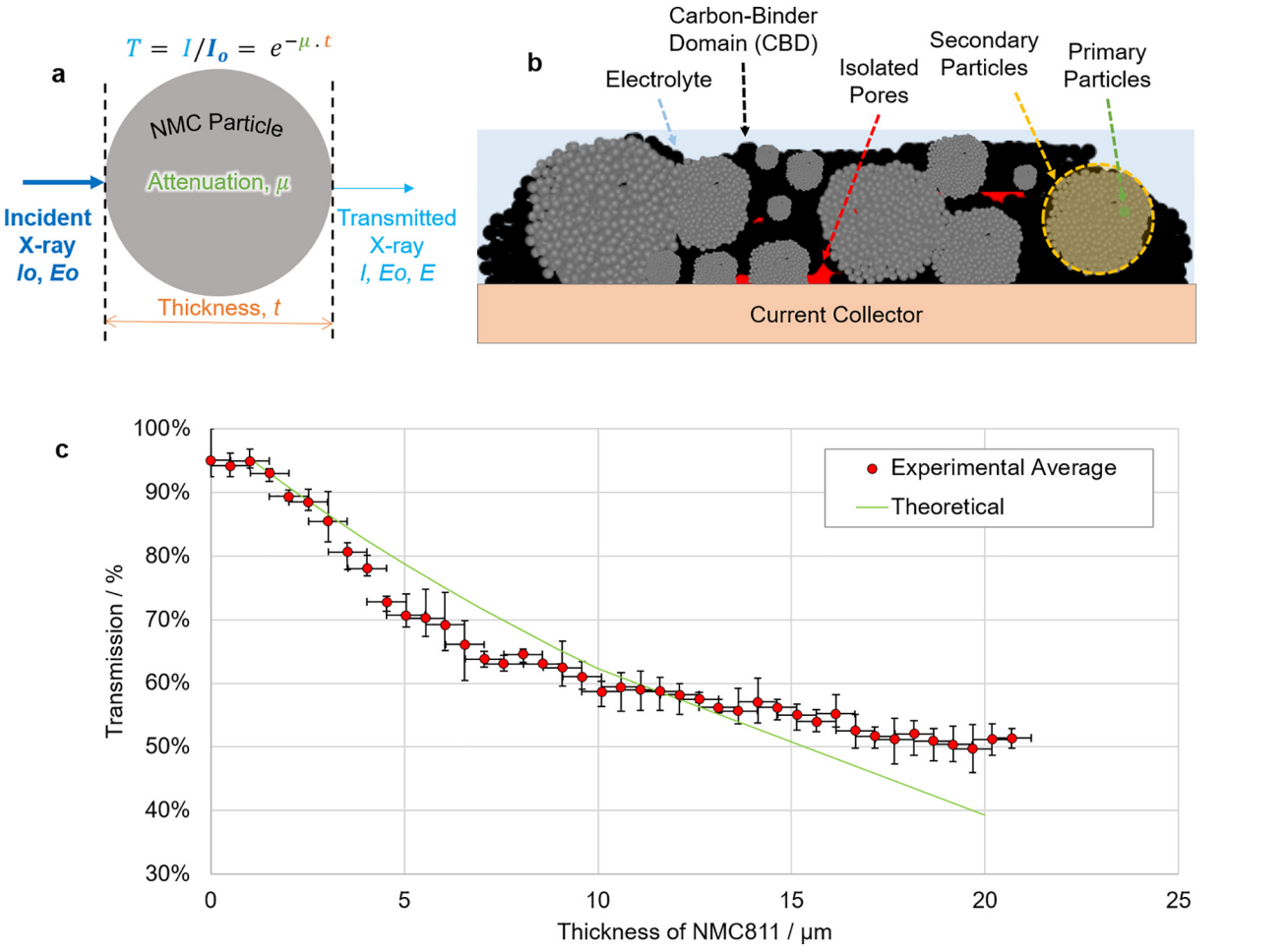

Fig. 4. Experimental validation: a) an ideal NMC particle with no internal voids and perfectly uniform structural density, b) an example of a more realistic structure and the causes for real-world deviation from theoretical transmission values, and c) experimental and theoretical transmission for an NMC811 particle.

Due to the strong relationship between incident energy and attenuation properties, Fig. 3 would provide a sufficient approximation in order to prepare samples for optimum image contrast in X-ray CT applications. However, as the sample of interest becomes more complex, e.g. multi-phase (Fig. 4b), the impact of the calculation assumptions should be considered. In order to test the validity of these predictions a single NMC811 particle was imaged using absorption-contrast, full-field X-ray radiography and CT. Using the reference-corrected radiographs the X-ray transmission through the particle could be calculated and using the X-ray CT tomograms this transmission was then allocated a corresponding sample thickness that the beam path travelled through before reaching the detector. This was conducted three times and a minimum, maximum and average transmission were calculated for each thickness. Fig. 4c presents the results with the transmission error calculated as the difference between the average and maximum or minimum and the thickness error defined as a constant value equal to the length of one pixel. Generally the experimental and theoretical values are very similar with only minor deviations. It should be noted that sample thickness was calculated as the length from one end of the particle to the other i.e. diameter. An internal void towards the centre of the particle may explain the deviation from theory towards thickness of 15–20 μm. Nonetheless, the theoretical prediction is certainly sufficient for experimental planning.

3.7. Influence of lithiation

If conducting in situ or operando imaging, the amount of Li and the crystallographic density of the structure can be expected to change. However, with respect to changes in the incident energy, or the presence of an impurity, the transmission change associated with lithiation mechanisms would be negligible. For example, consider a perfect NMC particle that is imaged using a 1, 10 and 100 keV incident beam energy for various degrees of lithiation. Table 7 outlines the X-ray mass attenuation coefficients for such a scenario, where lithiation is quantified by x which represents Li content within the $Li_{1-x}Ni_{0.8}Mn_{0.1}Co_{0.1}O_2$ structure. Clearly the influence of variations in the beam energy is considerably more substantial than the influence of lithiaiton state for the mass attenuation coefficient.

3.8. Materials applications

The experimentalists that go on to employ this framework may do so in order to conduct various types of characterisation methods. For instance, as well as methods that are absorption-based in nature, such as transmission spectroscopy [24], X-ray absorption is also important for other methods such as X-ray diffraction CT [25], energy-dispersive spectroscopy (EDS) [26] and X-ray photoelectron spectroscopy (XPS) [27]. An example being that X-ray fluorescence (XRF) characterisation is only possible if the fluorescence X-rays are able to escape the material; probing a low energy fluorescence spectrum may be purposeless if the signal receive has been too heavily attenuated. Consequently these calculations may be useful for many experiments, not limited to those that are purely transmission-based. Moreover, due to the ambiguous use of X-ray CT across many disciplines, this work may find use outside of the field of battery materials [28–31].

Table 7
An example of the influence of lithiation state (where x represents Li + content within $Li_{1-x}Ni_{0.8}Mn_{0.1}Co_{0.1}O_2$) upon the X-ray attenuation properties of NMC811 for three incident beam energies, X-ray mass attenuation coefficients presented in $cm^2\ g^{-1}$ (to 2 d.p.).

Lithiation state, x	1 keV	10 keV	100 keV
0.0	7333.73	122.56	0.32
0.2	7436.50	124.33	0.32
0.4	7542.29	126.15	0.32
0.6	7651.23	128.03	0.33
0.8	7763.46	129.96	0.33
1.0	7879.15	131.95	0.33

4. Conclusions

Ultimately, this work outlines the methodologies that allow X-ray CT experiments to be intelligently planned in order to optimise data quality, specifically for LIB cathode materials.

The procedure for using two well-established sources of attenuation data by Henke and Hubbell et al. has been outlined and their data compared. It was shown that both sources greatly corroborate one another and either may provide valuable attenuation information. The theoretical transmission values for four NMC chemistries was then reported for various sample sizes and incident X-ray energies, and finally, the optimum sample thickness and beam energy for NMC811 was reported as a quick reference guide in order to maximise X-ray CT image contrast.

Although these calculations may be used as a guide, one must acknowledge the influence of: deviations from linearity when interpolating with respect to beam energy; the degree of beam monochromaticity; internal porosity; the influence of multiple phases (e.g. CBD); and, the degree of lithiation. Although, each assumption has various degrees of influence, specific to the experiment. Experimental data was also compared to these theoretical predictions for the specific example of a Cr laboratory-based anode, providing sufficient corroboration for confident experimental planning.

As a closing remark, it should be noted that these methods are not limited to LIB materials but may be applied for X-ray CT to the wider field of materials analysis. We expect that the data presented will be a useful reference of battery researchers, whilst the articulate methodology will have interests across the wider fields of materials science and design engineering.

CRediT authorship contribution statement

T.M.M. Heenan: Conceptualization. **C. Tan:** Project administration. **A.J. Wade:** Project administration. **R. Jervis:** Project administration. **D.J.L. Brett:** Funding acquisition, Supervision. **P.R. Shearing:** Conceptualization, Funding acquisition, Supervision.

Declaration of competing interest

We confirm that this work is original, has not been published or simultaneously submitted for publication elsewhere, and that all authors have read and approved the text. There are no conflicts of interest with regards to this work.

Acknowledgements

The authors would like to acknowledge the EPSRC (EP/M014045/1), the Royal Academy of Engineering (CiET1718\59). This work was carried out with funding from the Faraday Institution (faraday.ac.uk; EP/S003053/1), grant number FIRG001. Access to the Zeiss Xradia 810 Ultra X-ray instrument was supported through (EP/K005030/1).

Data availability

The processed data required to reproduce these findings are available to download from the accompanying Data in Brief article [[23] – Data in Brief].

References

[1] D. Andre, S.J. Kim, P. Lamp, S.F. Lux, F. Maglia, O. Paschos, B. Stiaszny, Future generations of cathode materials: an automotive industry perspective, J. Mater. Chem. A 3 (13) (2015) 6709–6732, https://doi.org/10.1039/C5TA00361J.

[2] T.M. Heenan, C. Tan, J. Hack, D.J. Brett, P.R. Shearing, Developments in X-ray tomography characterization for electrochemical devices, Mater (2019) https://doi.org/10.1016/j.mattod.2019.05.019.
[3] P.J. Withers, X-ray nanotomography, Mater. 10 (12) (2017) 26–34, https://doi.org/10.1016/S1369-7021(07)70305-X.
[4] K. Jalkanen, J. Karppinen, L. Skogström, T. Laurila, M. Nisula, K. Vuorilehto, Cycle aging of commercial NMC/graphite pouch cells at different temperatures, Appl. 154 (2015) 160–172, https://doi.org/10.1016/j.apenergy.2015.04.110.
[5] S. Liu, L. Xiong, C. He, Long cycle life lithium ion battery with lithium nickel cobalt manganese oxide (NCM) cathode, J. of Power Sources 261 (2014) 285–291, https://doi.org/10.1016/j.jpowsour.2014.03.083.
[6] J.R. Wilson, J.S. Cronin, S.A. Barnett, S.J. Harris, Measurement of three-dimensional microstructure in a LiCoO2 positive electrode, J. of Power Sources 196 (7) (2011) 3443–3447, https://doi.org/10.1016/j.jpowsour.2010.04.066.
[7] Z. Liu, J.S. Cronin, K. Yu-chen, J.R. Wilson, K.J. Yakal-Kremski, J. Wang, K.T. Faber, S.A. Barnett, Three-dimensional morphological measurements of LiCoO2 and LiCoO2/Li (Ni1/3Mn1/3Co1/3) O2 lithium-ion battery cathodes, J. of Power Sources 227 (2013) 267–274, https://doi.org/10.1016/j.jpowsour.2012.11.043.
[8] P.R. Shearing, L.E. Howard, P.S. Jørgensen, N.P. Brandon, S.J. Harris, Characterization of the 3-dimensional microstructure of a graphite negative electrode from a Li-ion battery, Electrochem 12 (3) (2010) 374–377, https://doi.org/10.1016/j.elecom.2009.12.038.
[9] M. Ebner, F. Geldmacher, F. Marone, M. Stampanoni, V. Wood, X-ray tomography of porous, transition metal oxide based lithium ion battery electrodes, Adv. Energy Mater. 3 (7) (2013) 845–850, https://doi.org/10.1002/aenm.201200932.
[10] E. Maire, P.J. Withers, Quantitative X-ray tomography, Int. Mater. Rev. 59 (1) (2014) 1–43, https://doi.org/10.1179/1743280413Y.0000000023.
[11] P.R. Shearing, J. Golbert, R.J. Chater, N.P. Brandon, 3D reconstruction of SOFC anodes using a focused ion beam lift-out technique, Chem. Eng. Sci. 64 (17) (2009) 3928–3933, https://doi.org/10.1016/j.ces.2009.05.038.
[12] J.J. Bailey, T.M.M. Heenan, D.P. Finegan, X. Lu, S.R. Daemi, F. Iacoviello, N.R. Backeberg, O.O. Taiwo, D.J.L. Brett, A. Atkinson, P.R. Shearing, Laser-preparation of geometrically optimised samples for X-ray nano-CT, J. Microsc. 267 (3) (2017) 384–396, https://doi.org/10.1111/jmi.12577.
[13] C. Tan, S.R. Daemi, O.O. Taiwo, T.M.M. Heenan, D.J.L. Brett, P.R. Shearing, Evolution of electrochemical cell designs for in-situ and operando 3D characterization, Materials 11 (11) (2018) 2157, https://doi.org/10.3390/ma11112157.
[14] B.P. Flannery, H.W. Deckman, W.G. Roberge, K.L. D'AMICO, Three-dimensional X-ray microtomography, Science 237 (4821) (1987) 1439–1444, https://doi.org/10.1126/science.237.4821.1439.
[15] B.L. Henke, E.M. Gullikson, J.C. Davis, X-ray interactions: photoabsorption, scattering, transmission, and reflection at E= 50-30,000 eV, Z= 1-92, At. Data Nucl. Data Tables 54 (2) (1993) 181–342, https://doi.org/10.1006/adnd.1993.1013.
[16] J.H. Hubbell, S.M. Seltzer, Tables of X-Ray Mass Attenuation Coefficients and Mass Energy-Absorption Coefficients 1 keV to 20 MeV for Elements Z= 1 to 92 and 48 Additional Substances of Dosimetric Interest (No. PB-95-220539/XAB; NISTIR-5632), National Inst. of Standards and Technology-PL, Gaithersburg, MD (United States), 1995https://doi.org/10.18434/T4D01F Ionizing Radiation Div. NISTIR.
[17] M. Reiter, M. Krumm, S. Kasperl, C. Kuhn, M. Erler, D. Weiß, C. Heinzl, C. Gusenbauer, J. Kastner, Evaluation of transmission based image quality optimisation for X-ray computed tomography, Conference on Industrial Computed Tomography (ICT), ISBN: 978-3-8440-1281-1 2012, pp. 241–250.
[18] Y. Fujii, H. Miura, N. Suzuki, T. Shoji, N. Nakayama, Structural and electrochemical properties of LiNi1/3Co1/3Mn1/3O2–LiMg1/3Co1/3Mn1/3O2 solid solutions, Solid State Ionics 178 (11−12) (2007) 849–857, https://doi.org/10.1016/j.ssi.2007.03.002.
[19] Y.J. Gu, Q.G. Zhang, Y.B. Chen, H.Q. Liu, J.X. Ding, Y.M. Wang, H.F. Wang, L. Chen, M. Wang, S.W. Fan, Q.F. Zang, Reduction of the lithium and nickel site substitution in Li1+ xNi0. 5Co0. 2Mn0. 3O2 with Li excess as a cathode electrode material for Li-ion batteries, J. Alloys Compd. 630 (2015) 316–322, https://doi.org/10.1016/j.jallcom.2014.12.235.
[20] X. Zheng, X. Li, Z. Huang, B. Zhang, Z. Wang, H. Guo, Z. Yang, Enhanced electrochemical performance of Lini0. 6co0. 2mn0. 2o2 cathode materials by ultrasonic-assisted co-precipitation method, J. Alloys Compd. 644 (2015) 607–614, https://doi.org/10.1016/j.jallcom.2015.04.173.
[21] R. Jung, R. Morasch, P. Karayaylali, K. Phillips, F. Maglia, C. Stinner, Y. Shao-Horn, H.A. Gasteiger, Effect of ambient storage on the degradation of Ni-rich positive electrode materials (NMC811) for Li-ion batteries, J. Electrochem. Soc. 165 (2) (2018) A132–A141, https://doi.org/10.1149/2.0401802jes.
[22] M. Rousseau, Quantum theory of non-ideal photon detectors, J. Phys. A 8 (8) (1975) 1265, https://doi.org/10.1088/0305-4470/8/8/012.
[23] T.M.M. Heenan, C. Tan, A.J. Wade, Data on the Theoretical X-Ray Attenuation and Transmissions for Lithium-Ion Battery Cathodes, Data In Brief 2020 (Under editorial process).
[24] C. Chen, Y. Wei, Z. Zhao, Y. Zou, D. Luo, Investigation of the swelling failure of lithium-ion battery packs at low temperatures using 2D/3D X-ray computed tomography, Electrochim. Acta 305 (2019) 65–71, https://doi.org/10.1016/j.electacta.2019.03.038.
[25] D.P. Finegan, A. Vamvakeros, L. Cao, C. Tan, T.M.M. Heenan, S.R. Daemi, S.D.M. Jacques, A.M. Beale, M. Di Michiel, K. Smith, D.J.L. Brett, P.R. Shearing, C. Ban, Spatially resolving Lithiation in silicon–graphite composite electrodes via in situ high-energy X-ray diffraction computed tomography, Nano Lett. 19 (6) (2019) 3811–3820, https://doi.org/10.1021/acs.nanolett.9b00955.
[26] Z. Xu, Z. Jiang, C. Kuai, R. Xu, C. Qin, Y. Zhang, M.M. Rahman, C. Wei, D. Nordlund, C.J. Sun, X. Xiao, Charge distribution guided by grain crystallographic orientations in polycrystalline battery materials, Nat. Commun. 11 (1) (2020) 1–9, https://doi.org/10.1038/s41467-019-13884-x.
[27] C. Chen, T. Li, H. Tian, Y. Zou, J. Sun, Building highly stable and industrial NaVPO 4 F/C as bipolar electrodes for high-rate symmetric rechargeable sodium-ion full batteries, J. Mater. Chem. A 7 (31) (2019) 18451–18457, https://doi.org/10.1039/C9TA05396D.
[28] A. Plessis, I. Yadroitsava, I. Yadroitsev, Effects of defects on mechanical properties in metal additive manufacturing: a review focusing on X-ray tomography insights, Mater. Des. (2019) 108385, https://doi.org/10.1016/j.matdes.2019.108385.
[29] K. Naresh, K.A. Khan, R. Umer, W.J. Cantwell, The use of X-ray computed tomography for design and process modeling of aerospace composites: a review, Mater. Des. (2020), 108553. https://doi.org/10.1016/j.matdes.2020.108553.
[30] Y. Ma, Q. Zhang, Y. Wang, J. Hong, F. Scarpa, Topology and mechanics of metal rubber via X-ray tomography, Mater. Des. 181 (2019) 108067, https://doi.org/10.1016/j.matdes.2019.108067.
[31] J. Wang, Z. Guo, J.L. Song, W.X. Hu, J.C. Li, S.M. Xiong, On the growth mechanism of the primary silicon particle in a hypereutectic Al-20 wt% Si alloy using synchrotron X-ray tomography, Mater. Des. 137 (2018) 176–183, https://doi.org/10.1016/j.matdes.2017.09.062.